JOURNAL OF SPACECRAFT AND ROCKETS
Vol. 42, No. 1, January–February 2005

Geometric Analysis of Free-Return Trajectories Following a Gravity-Assisted Flyby

Ryan P. Russell* and Cesar A. Ocampo†
University of Texas at Austin, Austin, Texas 78712-1085

The purpose of this study is to systematically identify all feasible trajectories following a gravity-assisted flyby that immediately return to the flyby body with no intermediate maneuvers. Every class of possible transfer angles is considered including even-$n\pi$, odd-$n\pi$, and generic return orbits. Lambert's problem is solved for a desired time-of-flight range allowing the possibility for multiple spacecraft and celestial body revolutions. The solutions are expressed geometrically, and the resulting velocity diagram is a mission-planning tool with potential applications that include cycler trajectories and planetary moon tours. The generalized free-return solutions can be used to construct loitering orbits about one celestial body or transfers between multiple bodies. Several previously documented cycler trajectories are improved using the discussed solutions.

Nomenclature

a	=	semimajor axis
E	=	eccentric anomaly
F	=	focus of a transfer ellipse
M	=	number of complete revolutions made by the celestial body
N	=	number of complete revolutions made by the spacecraft
$\boldsymbol{r}$	=	position vector
T	=	period
t	=	time
$\boldsymbol{v}$	=	velocity vector
α, β, S	=	intermediate variables for Lambert's equation
γ	=	flight-path angle
$\theta, \delta, r_1, r_2, c$	=	input geometry for Lambert's equation; see Fig. 2a
μ	=	gravitational parameter of the primary
ψ	=	referencing angle for generic returns; see Fig. 12

Subscripts

B	=	celestial body
F	=	full-revolution return
f	=	final
H	=	half-revolution return
r	=	radial component
v	=	vacant focus
θ	=	transverse component
0	=	initial
∞	=	relative to celestial body before or after flyby

Introduction

FREE-RETURN trajectories have been the subject of many studies in the wake and anticipation of taking humans back to the moon and beyond.[1–3] Proven to be invaluable during the Apollo missions, free returns are useful for human exploration because they return to the original body, by design or as an abort option, without any powered maneuvers. Free returns are also useful on interplanetary missions or moon tours when consecutive flybys of the same body provide the appropriate timing and gravity-assisted maneuvers necessary to reach the next destination.

Half- and full-rev free returns, orbits with a transfer angle that is an odd or even integer multiple of π, respectively, are subsets of the general free-return transfer. First termed by Hollister,[4] half- and full-rev returns were originally defined such that the spacecraft and the celestial body were limited to a 1π or 2π transfer, respectively, and were used as stalling mechanisms in the construction of interplanetary cycler orbits. The half- and full-rev returns are of particular interest because the solution space for the targeting problem significantly increases if the transfer angle is an integer multiple of π. The extra degrees of freedom make it possible to find free-return solutions that are further constrained by the matching v_∞ conditions associated with gravity-assisted flybys. This concept has been applied to missions involving the moon,[5,6] Jupiter,[7] Venus,[8] and Mars.[9–11]

Free returns with transfer angles that are noninteger multiples of π are termed generic returns.[11] Unlike the half- or full-rev return, these nonresonant return orbits have no extra degree or degrees of freedom for a transfer with a given semimajor axis. However, because the multiple-revolution Lambert problem has many solutions there can exist several generic free returns, each with a different time of flight, for any given value of v_∞ at a flyby body.

Similar to Uphoff et al., this paper develops equations that govern even- and odd-$n\pi$ free returns.[7] Additionally, a detailed analysis using Lambert's equation provides further insight into the behavior of the solutions. Furthermore, a numeric method is presented to find all of the generic returns that are feasible following a flyby. The solutions for the $n\pi$ and generic returns are then combined onto one velocity diagram to provide a general design tool for multiple-flyby missions.

The first section gives an overview of Lambert's multiple revolution problem with an emphasis on $n\pi$ transfers. The next few sections outline methods to obtain semimajor axis values for full-rev, half-rev, and generic free returns, respectively. In the full-rev case, two methods are presented: a simple derivation based on orbital periods and a second more complete discussion based on Lambert's equation. In the half-rev and the generic case, Lambert's equation is used exclusively. The following section discusses the terminal velocity vectors that initiate free returns and expresses the solutions on a common flyby velocity diagram. Finally, an example application that uses $n\pi$ transfers to find several promising Earth–Mars cyclers is presented, followed by a discussion of conclusions and anticipated work.

Presented as Paper 2003-508 at the AAS/AIAA Astrodynamics Specialists Conference, Big Sky, MT, 3–7 August 2003; received 7 October 2003; revision received 20 January 2004; accepted for publication 21 January 2004.

*Ph.D. Candidate, Department of Aerospace Engineering, 210 East 24th Street, W. R. Woolrich Laboratories, 1 University Station, C0600; ryanrussell@mail.utexas.edu. Student Member AIAA.

†Assistant Professor, Department of Aerospace Engineering, 210 East 24th Street, W. R. Woolrich Laboratories, 1 University Station, C0600. Member AIAA.

Lambert's Problem

This section gives an introduction to Lambert's problem in general[12] and in the context of $n\pi$ transfers. The following sections will examine the application of Lambert's equation to $n\pi$ and generic free returns in more detail.

Half- and full-rev returns are specific cases of the classic Lambert targeting problem when the transfer angle is an integer multiple of π and 2π, respectively. It is well known that these cases lead to singularities when computing terminal velocity vectors using standard approaches. To understand the behavior of the solutions at these singularities, it is useful to look at them in the limit as they approach half- and full-rev returns.

The sum of the two chords connecting any point on a given ellipse to its two respective foci is a constant. From this familiar "tac and string" property, a diagram similar to that in Fig. 1a can be drawn to find all vacant foci locations for elliptic transfers from $\boldsymbol{r}_1$ to $\boldsymbol{r}_2$ given any sufficiently large value for semimajor axis.

The spheres centered at the tips of $\boldsymbol{r}_1$ and $\boldsymbol{r}_2$ are the locus of all vacant foci for ellipses of semimajor axis a, which contain the position vectors $\boldsymbol{r}_1$ and $\boldsymbol{r}_2$, respectively. The intersection of the two spheres is illustrated with a dotted circle in Figs. 1a and 1b. Note, in Fig. 1c, the intersection is a sphere rather than a circle. In the general case, if $\boldsymbol{r}_1$ is not parallel to $\boldsymbol{r}_2$ then the transfer plane is defined by the two position vectors. The intersection of this transfer plane and the dotted circle are the two points labeled as F_{v1} and F_{v2}. These are the two vacant foci locations for elliptic transfers from $\boldsymbol{r}_1$ to $\boldsymbol{r}_2$ with semimajor axis a. However, if the transfer angle is $(2N+1)\pi$, as is true for a half-rev return, then the transfer plane is no longer defined by the position vectors, and any point on the dotted circle on Fig. 1b is a valid location for the vacant focus. Because of the tac and string property, if the transfer angle is $2N\pi$ and $\boldsymbol{r}_1 \neq \boldsymbol{r}_2$ then there is just one point of intersection between the two spheres, and the only transfers possible are on a rectilinear ellipse. If the transfer angle is $2N\pi$ and $\boldsymbol{r}_1 = \boldsymbol{r}_2$, as is true for a full-rev return, then the two spheres merge into one. Thus, from Fig. 1c, any location on the sphere of radius $2a\text{-}r$ is a valid location for a vacant focus. In summary, there are only two vacant foci locations in the general case: one degree of freedom is required to specify the location for a half-rev return, and last, two degrees of freedom are required to specify the vacant focus location for a full-rev return.

Figure 2a shows the four transfers on the two possible ellipses in the general case. Figures 2b and 2c illustrate the transfers in the limit as they approach a half- and full-rev return, respectively. Note, the angle $\theta - 2N\pi$ is defined to always be less than or equal to π. Therefore, $\delta - 2N\pi$ is always defined to be greater than or equal to π.

Lambert's theorem states that the time of flight (TOF) connecting any two points on an elliptic orbit is a function only of its semimajor axis, the chord length between the two points, and the sum of the respective distances from the focus to the two points. Equation (1) summarizes the Lagrangian formulation generalized to include multiple revolutions of the primary as defined in Fig. 2a. Equation (1) holds true for all four transfers shown in Fig. 2. The quadrant ambiguities associated with the angles α and β uniquely characterize each of the four arcs. The solution associated with $\alpha = \alpha_0$ is termed "fast," whereas the solution associated with $\alpha = 2\pi - \alpha_0$ is termed "slow," indicating a slow solution has a longer time of flight than a fast solution given two transfers with a common semimajor axis:

$$\sqrt{\mu}\,\mathrm{TOF} = a^{\frac{3}{2}}[2N\pi + \alpha_{\mathrm{fast,slow}} - \beta - \sin(\alpha_{\mathrm{fast,slow}}) + \sin(\beta)] \quad (1)$$

where

$$\sin(\alpha_0/2) = \sqrt{S/(2a)}, \qquad \alpha_{\mathrm{fast}} = \alpha_0, \qquad \alpha_{\mathrm{slow}} = 2\pi - \alpha_0$$

$$\sin(\beta_0/2) = \sqrt{(S-c)/(2a)}$$

$$\beta = \beta_0 \quad \text{if transfer angle is} \quad \theta$$

$$\beta = -\beta_0 \quad \text{if transfer angle is} \quad \delta$$

$$S = (r_1 + r_2 + c)/2$$

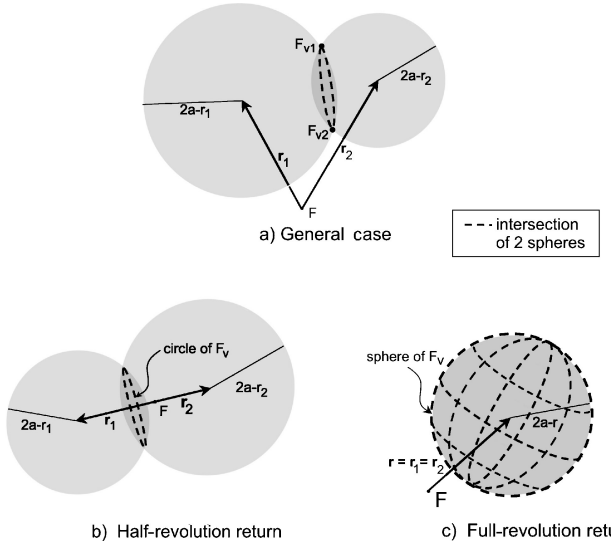

Fig. 1 Procedure to find vacant foci.

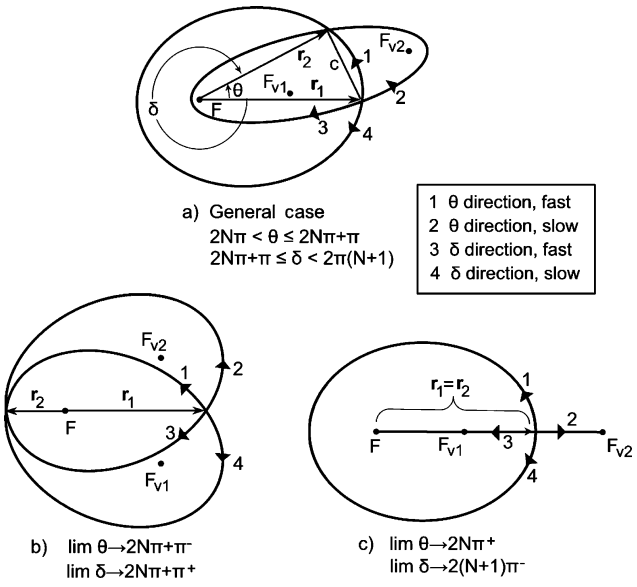

Fig. 2 Four possible arcs of Lambert's equation for a given *N*.

Generalized Full-Revolution Return Solutions

The generalized full-rev return is defined to be any trajectory that leaves a celestial body and returns directly to the same body after completing N revolutions of the primary while the celestial body completes M revolutions.

Expressions Based on Orbital Periods

Because the times of flight for full-rev returns are simple integer multiples of a celestial body's period, the governing equation of full-rev returns, Eq. (2), is derived by setting the times of flight for both the spacecraft and the celestial body to be equal:

$$M\left(2\pi\sqrt{a_B^3/\mu}\right) = N\left(2\pi\sqrt{a_F^3/\mu}\right) \quad (2)$$

Solving for a_F, the expression for the semimajor axis of a full-rev transfer becomes

$$a_F = a_B(M/N)^{\frac{2}{3}} \quad (3)$$

Table 1 Properties of Lambert solutions in the limit as $r_1 \to r_2$ [$\theta \to 2N\pi^+$, $\delta \to 2(N+1)\pi$]

Property	Transfer 1	Transfer 2	Transfer 3	Transfer 4
Transfer angle	$\theta \to 2N\pi^+$	$\theta \to 2N\pi^+$	$\delta \to 2(N+1)\pi^-$	$\delta \to 2(N+1)\pi^-$
Transfer ellipse period	T[a]	T	T	T
Time of flight	NT	$NT + \Delta t$[b]	$(N+1)T - \Delta t$	$(N+1)T$
e	$r/a - 1$	1	1	$r/a - 1$
Initial E	π^-	E_0[c]	$2\pi - E_0$	π^+
Final E	π^+	$2\pi - E_0$	E_0	π^-

[a] $T = 2\pi\sqrt{(a^3/\mu)}$. [b] $\Delta t = 2\pi - 4\sin^{-1}\{\sqrt{[r/(2a)]}\} + 2\sqrt{(2ar - r^2)}/a$. [c] $E_0 = \pi - \cos^{-1}[(r-a)/a]$.

Additional Insight from Lambert's Equation

Equation (2) can also be derived directly from Lambert's equation. The first step in deriving Eq. (1), shown in Eq. (4), is to subtract Kepler's equation applied to $\boldsymbol{r}_1$ from Kepler's equation applied to $\boldsymbol{r}_2$. The angles α and β are alternate parameters that can be shown to be functions of E_1 and E_2:

$$\sqrt{\mu}\,\mathrm{TOF} = a^{\frac{3}{2}}\{E_2 - E_1 - e[\sin(E_2) - \sin(E_1)]\} \tag{4}$$

When $\boldsymbol{r}_2 = \boldsymbol{r}_1$, and consequently $E_2 = E_1 + 2N\pi$, it becomes

$$\sqrt{\mu}\,\mathrm{TOF} = a^{\frac{3}{2}}(2N\pi) \tag{5}$$

Equation (5) is identical to Eq. (2) when $a = a_F$ and TOF is constrained to be M times the period of the celestial body.

The general form of Lambert's equation gives additional insight to the problem when observing the solutions in the limit as $\boldsymbol{r}_1 \to \boldsymbol{r}_2$. Examining Fig. 2a, as $\boldsymbol{r}_1 \to \boldsymbol{r}_2$ and consequently $\theta \to 2N\pi^+$ and $\delta \to 2(N+1)\pi^-$, the attracting focus, the tip of the position vectors, and the two empty foci become collinear as seen in Fig. 2c. The only possible ellipse with a position vector directly between foci F and F_{v2} is a rectilinear ellipse with $e = 1$. The only possible ellipse with foci F and F_{v1} that contains $\boldsymbol{r}$ is one whose apoapse occurs at $\boldsymbol{r}$; thus, $e = r/a - 1$. Both solutions are shown in Fig. 2c. In the limit, the two position vectors are very close, but never exactly parallel; thus, a transfer plane is defined, and the two vacant foci are unique, as illustrated in Fig. 2a. The transfers approach those illustrated in Fig. 2c, and properties of the solutions smoothly approach values as outlined in Table 1. However, when $\boldsymbol{r}_1 = \boldsymbol{r}_2$ exactly, the transfer plane is no longer defined, and the vacant focus can be anywhere on the sphere of possible locations, as seen in Fig. 1c. Thus, the rectilinear ellipse and the nonrectilinear ellipse in Fig. 2c represent just two points on the vacant foci sphere. Transfers 1 and 4 are specific cases of the solutions described by Eq. (2). However, transfers 2 and 3 are not described by Eq. (2) because the eccentric anomalies at the beginning and end of the transfers are different. Examining Fig. 2a, as $\boldsymbol{r}_1 \to \boldsymbol{r}_2$, it is clear that $E_0 \to E_f$ for transfers 1 and 4, but not for transfers 2 and 3. Expressions for these values, as well as other noteworthy properties for each of the four transfers, are given in Table 1.

Every point on the vacant foci sphere has a direct and retrograde transfer, each with a time of flight equal to a normalized value of $2N\pi$ time units (TU). However, the point on the sphere that is exterior to and collinear with F and $\boldsymbol{r}$ has two additional transfers because its associated ellipse is rectilinear. Equation (2) covers all of the solutions such that $E_0 = E_f$, including two of the four possible transfers on the rectilinear ellipse. The remaining two solutions on the rectilinear ellipse are transfers 2 and 3 as shown in Fig. 2c, where $E_0 \neq E_f$. For a given value of a_B, each set of M and N has an associated vacant foci sphere with radius $2a_F - r$. The two transfers on each ellipse associated with every point on the vacant foci sphere in addition to the two rectilinear solutions such that $E_0 \neq E_f$ comprise the set of all $M{:}N$ resonant transfers with a common semimajor axis.

In the limiting case when $\boldsymbol{r}_1 = \boldsymbol{r}_2$, then $c = 0$, $\alpha_0 = \beta_0$, and Eq. (1) simplifies to Eqs. (6–9), respectively, for transfers 1–4 shown in Fig. 2c:

$$\sqrt{\mu}\,\mathrm{TOF} = a^{\frac{3}{2}}2N\pi \tag{6}$$

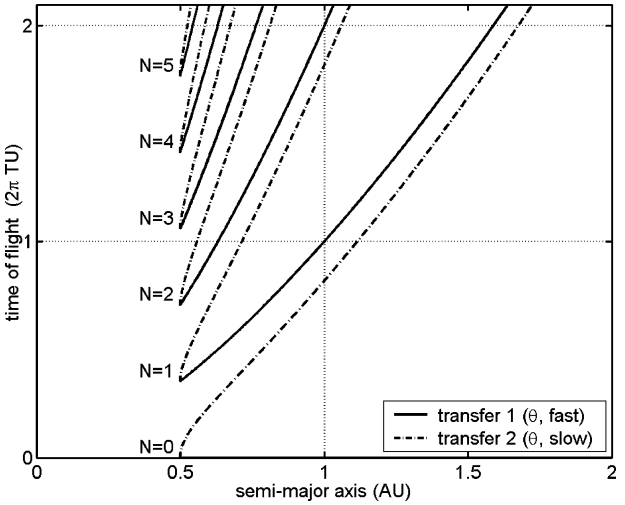

Fig. 3 Limit $r_1 \to r_2$. Lambert transfers using θ.

$$\sqrt{\mu}\,\mathrm{TOF} = a^{\frac{3}{2}}\left\{2\pi(N+1) - 4\sin^{-1}\left[\sqrt{r/(2a)}\right] + 2\sqrt{2ar - r^2}\Big/a\right\} \tag{7}$$

$$\sqrt{\mu}\,\mathrm{TOF} = a^{\frac{3}{2}}\left\{2N\pi + 4\sin^{-1}\left[\sqrt{r/(2a)}\right] - 2\sqrt{2ar - r^2}\Big/a\right\} \tag{8}$$

$$\sqrt{\mu}\,\mathrm{TOF} = a^{\frac{3}{2}}2\pi(N+1) \tag{9}$$

Equations (6) and (9) are identical to Eq. (5) except that N is phased by one in Eq. (9) because the transfer angle is δ rather than θ. As an example, suppose it is desirable to traverse one revolution of the primary. If transfer 1 is used, the associated N is one because the transfer angle θ approaches $2\pi^+$, and a full revolution is completed as $\boldsymbol{r}_1 \to \boldsymbol{r}_2$. However, if transfer 4 is used the associated N is zero because the transfer angle δ approaches $2\pi^-$, and a full revolution is not reached as $\boldsymbol{r}_1 \to \boldsymbol{r}_2$.

Figures 3 and 4 plot the four time-of-flight vs semimajor axis curves expressed in Eqs. (6–9) representing all four full-rev transfer arcs. The plots were generated using canonical variables with $\mu = 1$ AU^3/TU^2, $r = 1$ AU, where AU is an astronomical unit, and $N = 0 \to 5$. Figure 5 is the two prior figures plotted on the same axes. Note that the transfer 1 curve is identical to the transfer 4 curve when N is phased by one, as evidenced from Eqs. (6) and (9). Also, the values of the TOF($a_{\min}$) and $\partial\mathrm{TOF}/\partial a(a_{\min})$ are equal for the transfer 2 and 3 curves when N is phased by one. This is easily shown using Eqs. (7) and (8) and recognizing that $a_{\min} = S/2$.

Figure 5 contains all time-of-flight and semimajor axis information for transfers that make $2N\pi$ revolutions of the primary. More information is necessary to pick out the specific transfers that leave and return to a particular celestial body. Clearly, the trajectory of the celestial body must also lie on one of the curves in Fig. 5. Because a rectilinear ellipse is not a physically realistic solution, the trajectory of the body can only be a transfer 1 or 4 curve. A vertical dotted line is drawn at $a = a_B$. An example value of $a_B = 1$ AU is used in the figures. The intersections of this vertical line with the transfer 1 and 4 curves locate the solutions that correspond to the trajectory of the celestial body. The horizontal dotted lines are then drawn at each

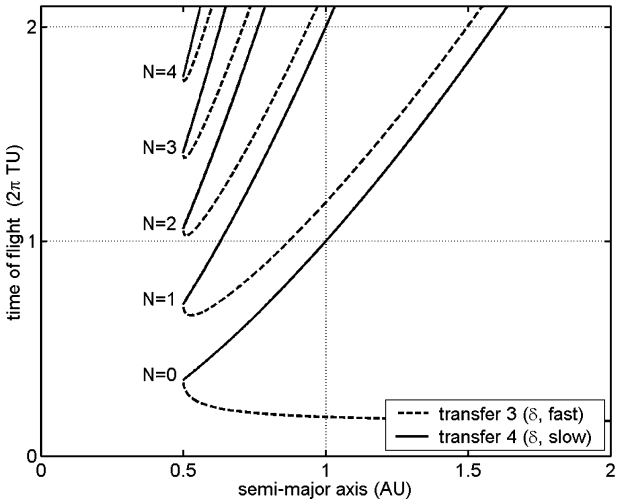

Fig. 4 Limit $r_1 \rightarrow r_2$. Lambert transfers using δ.

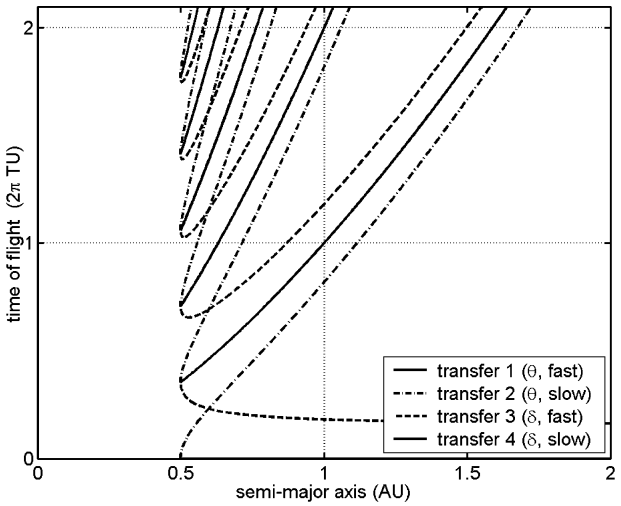

Fig. 5 Limit $r_1 \rightarrow r_2$. All Lambert transfers.

of the intersections. Each integer multiple of the celestial body's period is associated with a horizontal dotted line, corresponding to values of M in Eq. (2). Finally, the intersections of the transfer lines with these horizontal lines represent specific semimajor axis values that will yield orbits that return to the body after N revolutions.

For example, there are five values of semimajor axis that yield nonrectilinear orbits that return after the celestial body makes two complete revolutions of the primary. Examining Fig. 5, the five values for the semimajor axis are found by locating the intersections of the top horizontal dotted line with the transfer 1 and 4 curves. The values are identical to those obtained with Eq. (3).

Generalized Half-Revolution Return Solutions

The generalized half-rev return is any trajectory that leaves a celestial body and returns directly to the same body after completing $N + 1/2$ revolutions of the primary. When $N = 0$, the half-rev return is also known as a backflip[6] trajectory. Examining Fig. 1b, when the transfer angle is $(2N + 1)\pi$, any point on the dotted circle is a valid location for the vacant focus. The alternate focus locations represent a rotation of the transfer orbit about the position vectors. Thus, the shape of the transfer ellipse is fixed, but a free parameter is required to specify the transfer plane.

A simple expression similar to Eq. (2) is not available for the half-rev return because the times of flight are not simple multiples of the orbital periods. Lambert's equation is necessary for the analysis. In the limit as the transfer angle approaches $2N\pi + \pi$, as seen in Fig. 2b, the first and second Lambert transfers become mirror images of the third and fourth, respectively. Similar to the full-rev discussion, the two vacant foci of the ellipses in Fig. 2b correspond to specific opposing locations on the dotted circle in Fig. 1b:

$$\sqrt{\mu}\,\mathrm{TOF} = a^{\frac{3}{2}}\left\{2N\pi + 2\sin^{-1}\left[\sqrt{(r_1 + r_2)/2a}\right] - \sqrt{(2a - r_1 - r_2)(r_1 + r_2)}\Big/a\right\} \tag{10}$$

$$\sqrt{\mu}\,\mathrm{TOF} = a^{\frac{3}{2}}\left\{2\pi(N + 1) - 2\sin^{-1}\left[\sqrt{(r_1 + r_2)/2a}\right] + \sqrt{(2a - r_1 - r_2)(r_1 + r_2)}\Big/a\right\} \tag{11}$$

Equation (1) simplifies to Eq. (10) for transfers 1 and 3 and simplifies to Eq. (11) for transfers 2 and 4. The solution is indifferent to using the δ or θ direction because $\beta_0 = -\beta_0 = 0$ in Eq. (1). Figure 6 shows the time-of-flight vs semimajor axis plots for a sample half-rev geometry using $\mu = 1$ AU^3/TU^2, $r_1 = r_2 = a_B = 1$ AU, and $N = 0 \rightarrow 5$. In canonical terms, one revolution for the celestial body is 2π TU. Thus, the vertical axis is labeled in celestial body periods. In Fig. 6, the semimajor axes that correspond to half-rev solutions are denoted by the intersections of the dotted lines and the transfer curves. Note that $r_1 = r_2$, $a_B = a_{\min}$, and the horizontal lines occur exactly at half-periods, indicating the celestial body is in a circular orbit. As an example, if a spacecraft leaves a celestial body at $\boldsymbol{r}_1$ and the time of flight is 4.5 celestial body periods then there are nine semimajor axis values that yield transfers that will reencounter the body at $\boldsymbol{r}_2$. The two solutions from $N = 4$ are more easily seen in Fig. 7.

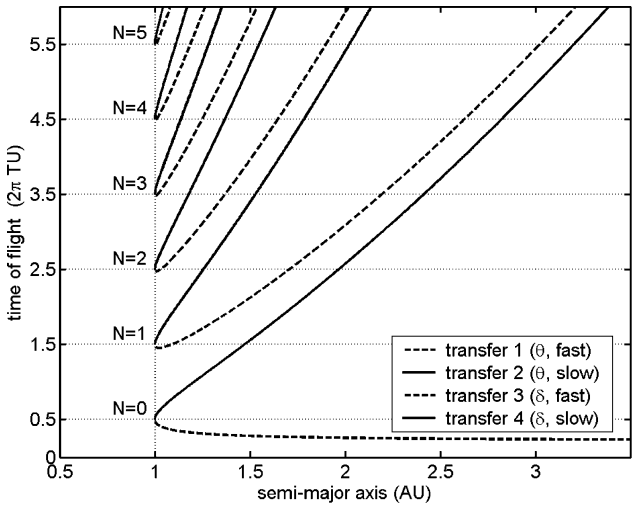

Fig. 6 Half-rev solutions, $|\boldsymbol{r}_1| = |\boldsymbol{r}_2|$.

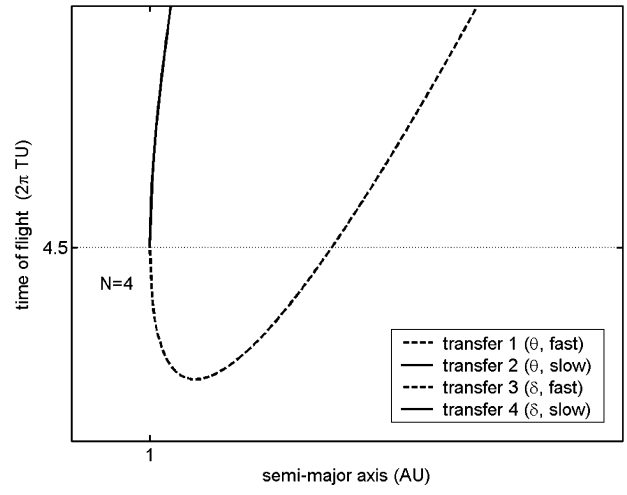

Fig. 7 Zoom view of the $N = 4$ curve.

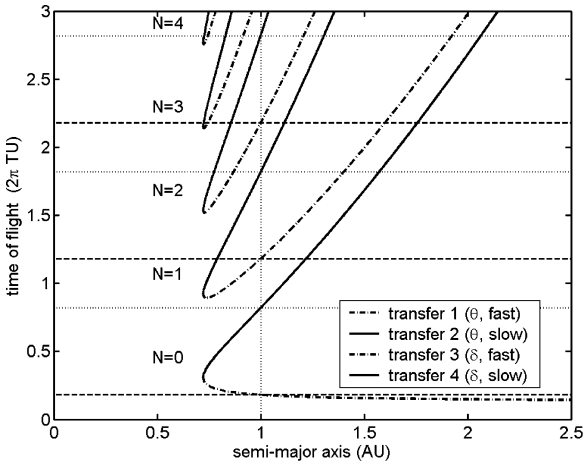

Fig. 8 Half-rev solutions, $|r_1| \neq |r_2|$.

For the special case of $a_B > a_{\min}$ and $r_1 = r_2$, the celestial body must be in an elliptic orbit with its line of apses perpendicular to the terminal position vectors. In this case, the vertical dotted line corresponding to a_B should be moved accordingly in Fig. 6, and the procedure to find the half-rev solutions is similar to that described next when $r_1 \neq r_2$.

Figure 8 represents the more general case where $r_1 \neq r_2$. For this example, $r_2 = 0.45$ AU and the other parameters remain unchanged. Before identifying solutions that return to the body, it is necessary to specify whether the body is on a fast- or slow-path solution. If the body is on a fast path, then the times of flight corresponding to half-rev returns are denoted by the intersections of the vertical dotted line, positioned at $a = a_B$, with the fast transfer curves. These intersections are marked with horizontal dashed lines, each with an associated value of M that increases with TOF. If the body is on a slow path, the intersections of the solution curves with the horizontal dotted lines indicate the half-rev return times of flight. Notice that successive dashed and dotted lines are respectively spaced by the period of the celestial body. The bottom dashed and dotted lines correspond to the $M = 0$ fast- and slow-path solutions, respectively.

For example, from Fig. 8, suppose the celestial body with $a_B = 1$ is on a fast-path transfer, then there are seven $M = 2$ solutions that return to the body. The $M = 2$ solutions are marked by the dashed line with TOF $= 2.18 \times 2\pi$ TU. The two $N = 3$ intersections occur at $a = 0.73$ and 0.75 AU. The two $N = 2$ intersections occur at $a = 0.86$ and 1 AU. Note the latter corresponds to the path of the celestial body. The two $N = 1$ intersections occur at $a = 1.11$ and 1.60 AU. Last, the one $N = 0$ intersection occurs at $a = 1.76$ AU.

Generic Free-Return Solutions

Generic free returns consist of all free returns that are not even- or odd-$n\pi$ transfers. Suppose a celestial body is located at $\boldsymbol{r}_1$ along its orbit, as seen in Fig. 2a. For sufficiently large times of flight, multiple generic-return solutions exist, including the path of the body itself. For a given $0 < \theta < \pi$, the input geometry, or δ, r_1, r_2, and c, can be easily calculated for the Lambert problem that connects the body's initial and final positions. Using these values, a plot similar to Fig. 8 can be generated for each transfer angle using Eq. (1). However, for the generic returns, the plot will have four distinct sets of solutions corresponding to transfers 1–4 as opposed to the two seen in Fig. 8. An example plot generated with $\theta = \pi/4$, $r_1 = r_2 = 1$ AU, and $\mu = 1$ AU^3/TU^2 is given in Fig. 9.

The solutions using θ, or transfers 1 and 2, represent either direct or retrograde transfers, whereas solutions using δ, or transfers 3 and 4, represent the opposite, depending on the motion of the celestial body. A similar procedure as just described in the half-revolution case is required to solve for all semimajor axis values that correspond to generic-return solutions that initiate and terminate at a particular body. The process can be repeated for every value of $0 < \theta < \pi$ at any desired interval. Each plot contains all solutions for $\theta + 2M\pi$ and $\delta + 2M\pi$, where M is any integer.

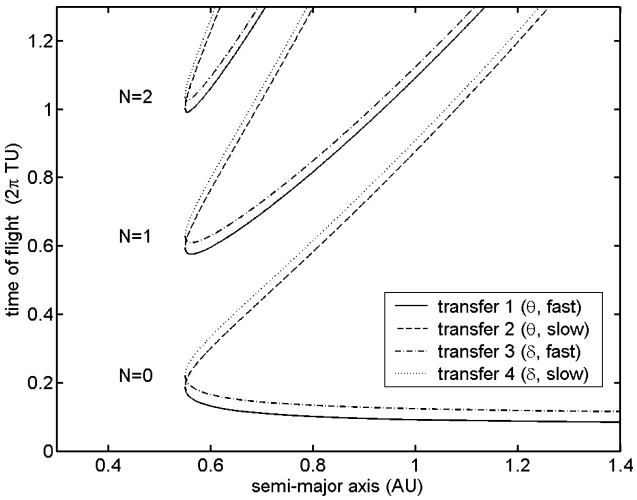

Fig. 9 Example generic-return solutions.

Flyby Velocity Diagrams

The preceding sections provide methods to obtain semimajor axis values for all three types of free returns: full-rev, half-rev, and generic. Based on these values, this section discusses the outbound velocity vectors required to initiate the free returns and expresses the solutions on three-dimensional velocity diagrams.

Full-Revolution Velocity Diagrams

If a spacecraft leaves a celestial body on an orbit with the semimajor axis a_F, obtained from Eq. (3) or a plot similar to Fig. 5, then it will return directly after it completes N revolutions. Equation (12) is the vis-viva equation solved for spacecraft velocity magnitude. Inserting Eq. (3) into Eq. (12) gives Eq. (13) and restates the constraint in terms of velocity magnitude:

$$v_F = \sqrt{2\mu/r - \mu/a_F} \tag{12}$$

$$v_F = \sqrt{2\mu/r - \mu(N/M)^{\frac{2}{3}}/a_B} \tag{13}$$

Thus, if a spacecraft leaves a celestial body with the speed relative to the primary given by Eq. (13) then it will return after it completes N revolutions. The constraints described in Eqs. (3) and (13) are identical to the constraint that the absent focus must lie on the sphere of intersection from Fig. 1c. The scalar nature of Eq. (13) is significant because the direction of the velocity magnitude is unconstrained. This provides a convenient method to parameterize the two degrees of freedom associated with full-rev returns. Feasible values for N, M, r, μ, and a_B are combinations such that v_F from Eq. (13) is nonimaginary. For fixed values of M, r, μ, and a_B, N can vary from 1 to $N_{\max}$.

If a celestial body with semimajor axis a_B is located a distance r from the primary, then for a given M and N the locus of all spacecraft velocity vector tips that initiate full-rev returns is a sphere. The full-rev sphere is centered at the base of the body's velocity and has a radius of v_F. If a spacecraft approaches a body with an arbitrary hyperbolic speed and direction, the locus of all feasible points for the velocity after an unpowered gravity-assisted flyby is the surface of a sphere with radius v_∞ centered at the tip of the body's velocity. This is the common three-dimensional velocity diagram for a gravity-assisted maneuver. A sample diagram with these spheres is illustrated in Fig. 10. Canonical units were used to generate the figure with $\mu = 1$ AU^3/TU^2, $r = a_B = 1$ AU, $N = 7$, $M = 4$, and $v_\infty = 0.5$ AU/TU. The right-handed coordinate system chosen for illustration and analysis of these diagrams is centered at the tip of $\boldsymbol{v}_B$ with the z axis aligned with $\boldsymbol{v}_B$ and the y axis opposed to the celestial body's angular momentum vector. The sphere centered at

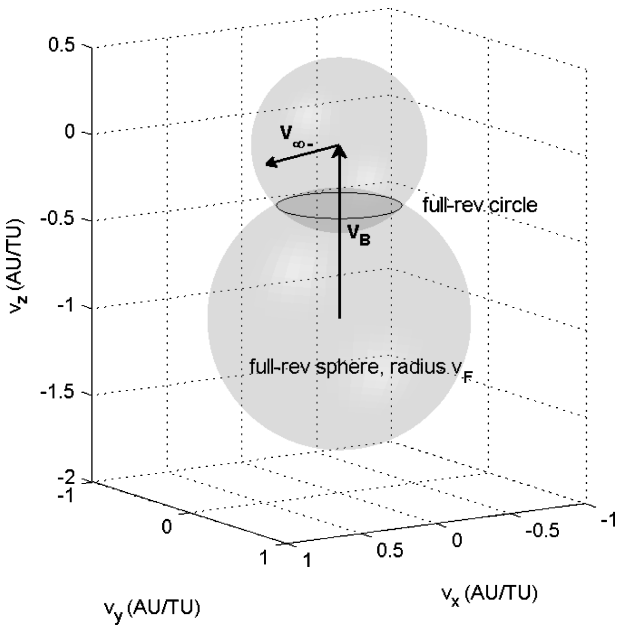

Fig. 10 Full-rev velocity diagram: $N = 7$ and $M = 4$.

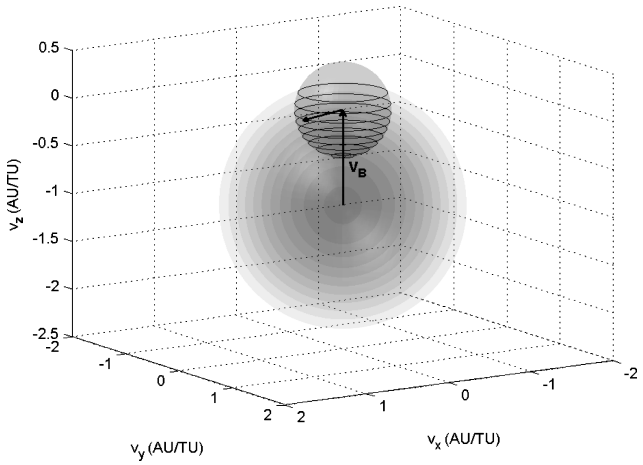

Fig. 11 Full-rev velocity diagram: $N = 1 \rightarrow 11$ and $M = 4$.

the base of $\boldsymbol{v}_B$ is the full-rev sphere associated with Eq. (13). The sphere centered at the tip of $\boldsymbol{v}_B$ is the v_∞ sphere. The circle marks the intersection of the two spheres. If $\boldsymbol{v}_{\infty+}$ is located anywhere on this circle, the spacecraft and body will reencounter after completing seven and four revolutions, respectively. Figure 11 illustrates all of the full-rev spheres associated with $M = 4$. It is clear that nine of the full-rev spheres intersect with the v_∞ sphere to form full-rev circles. If $\boldsymbol{v}_{\infty+}$ is located on any of the full-rev circles illustrated in Fig. 11, then the spacecraft and body will reencounter after the body completes four revolutions. $N_{\max}$ is 11 in this example. However, all 11 spheres do not necessarily intersect with the v_∞ sphere. Equation (14) is a logical expression that must be true for an intersection to exist for a given v_B, v_F, and v_∞:

$$\{v_F \geq |v_B - v_\infty|\}, \qquad \{v_F \leq v_B + v_\infty\} \tag{14}$$

The equations describing the surface of the v_∞ and v_F spheres are given by Eqs. (15) and (16):

$$x^2 + y^2 + z^2 = v_\infty^2 \tag{15}$$

$$x^2 + y^2 + (z + v_B)^2 = v_F^2 \tag{16}$$

Eliminating x and y, Eq. (17) gives the z value for the full-rev circle of intersection:

$$z_F = \left(v_F^2 - v_\infty^2 - v_B^2\right)/2v_B \tag{17}$$

Half-Revolution Velocity Diagrams

The f and g functions are typically used to solve for the terminal velocity vectors on a transfer with a known value for semimajor axis. However, singularities exist in these functions when the transfer angle is an integer multiple of π. For full-rev returns, it was determined that the terminal velocity vectors can be located anywhere on a sphere with radius given in Eq. (13). For a half-rev return, the components of the outbound terminal velocity vector are derived by Battin[13] and expressed in Eqs. (18) and (19):

$$v_{\mathrm{Hr}}^2 = \mu[2/(r_1 + r_2) - 1/a] \tag{18}$$

$$v_{H\theta}^2 = 2\mu r_2 \left/ \left(r_1^2 + r_1 r_2\right)\right. \tag{19}$$

Figure 12 is a diagram of the velocity vector $\boldsymbol{v}_H$ in the ecliptic plane that produces a half-rev return orbit. The x axis of the primed coordinate system is aligned with $\boldsymbol{r}_B$ while the unprimed z axis is aligned with $\boldsymbol{v}_B$. Because the transfer plane is not specified, $\boldsymbol{v}_H$ can be rotated by any angle about $\boldsymbol{r}_B$, and the resulting velocity vector will initiate a half-rev return. Notice the squares in the component equations indicate double valued solutions. If the solution is a fast transfer, then it initially moves toward periapse; thus, the radial component of the velocity that initiates the return must be negative. The opposite is true for a slow transfer. Examining Fig. 2b, it is clear that the two fast transfers, 1 and 3, have negative initial radial components for velocity. It is also clear that the two slow transfers, 2 and 4, initially move toward apoapse and have positive initial radial components of velocity. For the transverse component, the positive and negatives values produce half-rev returns because the transfer plane is undefined. The positive value, however, is used to reference the zero point for the free angle that specifies the transfer plane.

Examining Fig. 12, the rotation of $\boldsymbol{v}_H$ about $\boldsymbol{r}_B$ forms a cone. The base of this cone, the half-rev circle, is the locus of all terminal velocity vector tips that lead to a half-rev return with a given semimajor axis. Uphoff and Crouch[6] refer to this cone as the "equal gamma cone."

Figure 13 is an example velocity diagram that contains a half-rev circle. Generated using information from Fig. 6, it includes $\boldsymbol{r}_B$, $\boldsymbol{v}_B$, $\boldsymbol{v}_{\infty-}$, the v_∞ sphere, and the half-rev circle that corresponds to the slow $N = 2$ solution with a time of flight of 3.5 celestial body periods. The slow $N = 2$ curve from Fig. 6 has a semimajor axis of 1.18 AU when the time of flight is 3.5 periods. Inserting this into Eqs. (18) and (19) gives $v_{\mathrm{Hr}} = 0.153$ AU/TU and $v_{H\theta} = 1$ AU/TU.

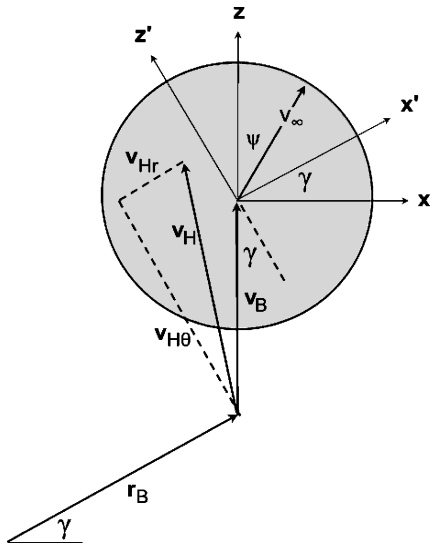

Fig. 12 Outbound velocity components for half-rev free returns.

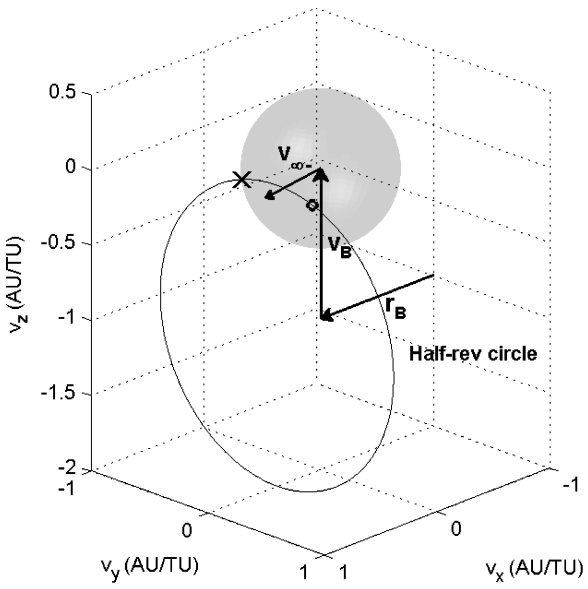

Fig. 13 Half-rev velocity diagram: $M = 3.5$ and $N = 2$ slow.

Because $a = 1.18$ AU is a slow solution, meaning that it comes from the upper of the two $N = 2$ curves, v_{Hr} must be positive.

In general, the plane of any half-rev circle is perpendicular to $\boldsymbol{r}_B$. Particular to this example, the plane of the half-rev circle in Fig. 13 is the y–z plane because the celestial body is in a circular orbit. It is clear from Fig. 12 that the directions of v_{Hr} and $v_{H\theta}$ are aligned with the x and z axes, respectively, when the flight-path angle is zero.

The v_∞ sphere and the half-rev circle intersect at two locations, one below and one above the ecliptic plane, or the x–z plane. They are marked with an "x" and "o" respectively. These are the two feasible locations for $\boldsymbol{v}_{\infty+}$ following an unpowered flyby that will initiate this particular half-rev return. From Fig. 12, in terms of the primed coordinates the expressions describing the half-rev circle are given by Eqs. (20) and (21):

$$(y')^2 + [z' + v_B \cos(\gamma)]^2 = v_{H\theta}^2 \tag{20}$$

$$x' = v_{\mathrm{Hr}} - v_B \sin(\gamma) \tag{21}$$

The v_∞ sphere, expressed in the prime coordinates, is

$$(x')^2 + (y')^2 + (z')^2 = v_\infty^2 \tag{22}$$

Solving for x', y', and z' from Eqs. (20–22) gives the location of the two half-rev points of intersection. The coordinates, expressed in the unprimed variables, are given in Eqs. (23–25):

$$x = [v_{\mathrm{Hr}} - v_B \sin(\gamma)]\cos(\gamma) + K \sin(\gamma)/[2v_B \cos(\gamma)] \tag{23}$$

$$y = \pm\sqrt{v_\infty^2 - [v_{\mathrm{Hr}} - v_B \sin(\gamma)]^2 - K^2/[2v_B \cos(\gamma)]^2} \tag{24}$$

$$z = [v_{\mathrm{Hr}} - v_B \sin(\gamma)]\sin(\gamma) - K/(2v_B) \tag{25}$$

where

$$K = 2v_{\mathrm{Hr}} v_B \sin(\gamma) + v_B^2[1 - 2\sin^2(\gamma)] - v_{H\theta}^2 - v_{\mathrm{Hr}}^2 + v_\infty^2$$

Continuing with the example, it is clear from Fig. 6 that a time of flight of 3.5 periods yields seven corresponding solutions for semimajor axis. Thus, for this one time of flight there are seven half-rev circles. All seven are illustrated in Fig. 14. The circles form a tube-like structure with a radius $v_{H\theta}$ and centerline $\boldsymbol{r}_B$. Equation (19) indicates that $v_{H\theta}$ is not a function of a or TOF. Therefore, the diameter of the tube is a constant for a specified μ, r_1, and r_2. For this example, it is clear that only three out of the seven circles intersect with the $v_\infty = 0.5$ AU/TU sphere. For an intersection to exist, the y coordinate given in Eq. (24) must be nonimaginary.

Table 2 $N = 1$ solutions

No.	Ψ, deg	TOF (flyby body periods)	a, AU	N, rev
1	−139.5	0.899	0.540	+ 1
2	−96.33	1.571	1.245	− 1
3	−81.04	2.406	2.146	− 1
4	−73.19	3.336	3.114	− 1
5	−68.37	4.299	4.099	− 1
6	−65.06	5.276	5.090	− 1
7	74.29	5.655	2.941	+ 1
8	78.20	4.621	2.433	+ 1
9	83.74	3.567	1.920	+ 1
10	92.73	2.469	1.392	+ 1
11	114.0	1.250	0.804	+ 1

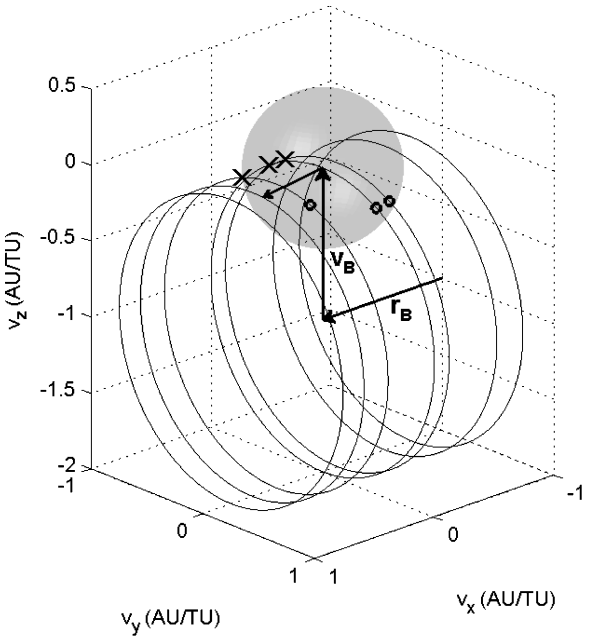

Fig. 14 Half-rev velocity diagram: $M = 3.5$.

Generic Free-Return Velocity Diagrams

The outbound terminal velocity vector for generic free returns can be easily calculated using the f and g functions.[12] As an example, the outbound velocity vectors are calculated for all generic free-returns with times of flight up to six celestial body periods for a body in a circular orbit. Note, because the body is in a circular orbit, it is not necessary to specify its departure location along the orbit. The multiple-revolution Lambert problem is solved at half-degree intervals, and the coordinates for each resulting outbound velocity are recorded. Only direct (posigrade) solutions are included. All solutions corresponding to $N = 1$, meaning the spacecraft makes between one and two revolutions of the primary, are displayed in Fig. 15.

Note that all generic-return solutions are in the ecliptic plane or x–z plane in the unprimed coordinate system defined in Fig. 12. The arbitrary v_∞ sphere and the $N = 1$ solutions intersect at the points denoted by the large dots. Because the problem is solved at discrete half-degree intervals, the apparent lines are not continuous. The solution properties of the intersection points are interpolated linearly between the two bordering points with the v_∞ sphere. Table 2 gives the interpolated results for the 11 intersection points for this example. The angular coordinate ψ denotes its location in the ecliptic plane on the v_∞ sphere referenced to $\boldsymbol{v}_B$, with positive being in the direction of $\boldsymbol{r}_B$.

Figure 16 shows all possible generic return solutions for N values of $1 \ldots N_{\max}$. The 75 intersection points for the example v_∞ sphere are also shown. The spacing between the points seen in Fig. 16 is a function of the transfer angle interval. The half-degree interval was chosen to give good resolution, yet still illustrate that the lines are

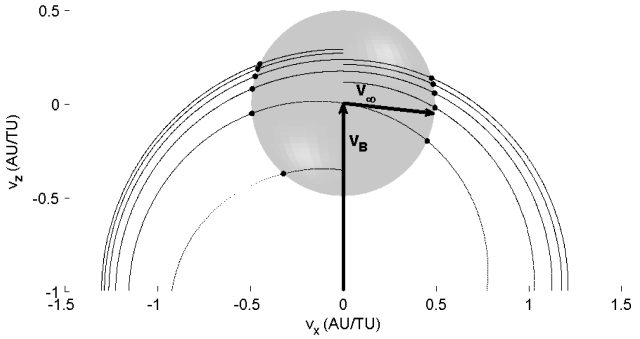

Fig. 15 $N = 1$ solutions, TOF = 0 → 6 flyby body periods.

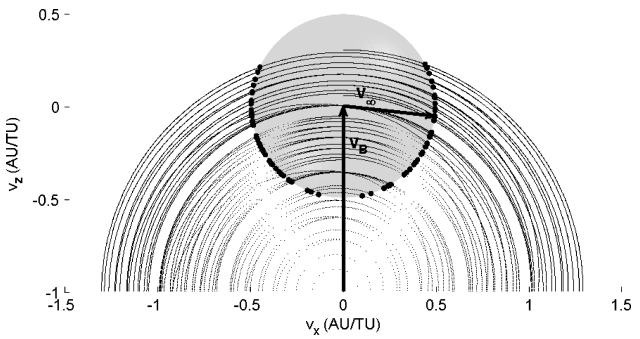

Fig. 16 All solutions $N = 1 \rightarrow 15$. TOF = 0 → 6.

composed of many points. In some regions of the velocity space, the point density is significantly less than others. This indicates regions of less stable solutions, meaning the departure directions at Earth are more sensitive to the time of flight in these regions. A more detailed analysis of the solution behavior in these regions is left to future work. When solving for the intersection points, a transfer angle interval of 1/24 deg is used to decrease the probability that any solutions are skipped.

Remember that each of the small dots represents a unique transfer with an associated time of flight ψ and semimajor axis. These values are also interpolated when solving for the intersection points. For each point, Figs. 17 and 18 plot ψ as a function of v_∞, whereas Figs. 19 and 20 plot TOF as a function of v_∞. With this interpolation technique, all possible generic returns can be found for any value of v_∞.

Flyby Diagrams Containing All Free-Return Solutions

Although Figs. 11, 14, and 16 illustrate a few of the full-rev, half-rev, and generic free-return solutions, it might be desirable for a given value of of v_∞ to obtain all free-return solutions including every possible combination of multiple revolutions by the spacecraft and the body. Examining the figures with velocity diagrams, the radius of the v_∞ spheres used for these examples is half the magnitude of the celestial body's circular velocity. This value was exaggerated intentionally for graphical purposes. Typically it is more desirable to have significantly lower hyperbolic energy levels; thus, the radius for a more realistic v_∞ sphere might only be one-tenth to one-fourth of the body's velocity. Clearly, a v_∞ sphere with a smaller radius will have fewer intersection locations for free-return solutions. An example diagram with a more realistic v_∞ value is shown in Fig. 21. This map contains all possible locations for $\boldsymbol{v}_{\infty+}$ following a flyby such that the spacecraft will return ballistically for times of flight up to six celestial body periods.

Similar to the preceding diagrams, Fig. 21 was generated using a celestial body in a circular orbit. It is a projection view of the v_∞ sphere along the y axis; thus, the full-rev circles appear as horizontal lines, and each set of the two half-rev points appear as an x underneath an o. The labels indicate time of flight in celestial body periods. The generic-return dots are labeled directly, whereas the half-rev points and full-rev circles are labeled along the top and to the right of the plot, respectively. The locations and properties of each of the generic returns interpolated using the data from Figs. 17–20 are shown in Table 3.

Table 3 Details of generic-return solutions in Fig. 21

No.	Ψ, deg	TOF (flyby body periods)	a, AU	N[a], rev
1	−158.6	5.944	0.668	+8
2	−158.2	3.943	0.669	+5
3	−157.0	1.939	0.671	+2
4	−139.9	4.882	0.718	+6
5	−131.0	5.843	0.754	+7
6	−130.1	2.838	0.758	+3
7	−120.4	3.783	0.809	+4
8	−115.0	4.745	0.842	+5
9	−111.5	5.718	0.866	+6
10	−93.07	5.534	1.022	−5
11	−92.58	4.529	1.026	−4
12	−91.80	3.520	1.034	−3
13	−90.40	2.504	1.049	−2
14	−86.96	1.466	1.086	−1[b]
15	−72.55	5.325	1.263	−4
16	−66.53	4.278	1.347	−3
17	−55.51	3.208	1.515	−2
18	−45.64	5.158	1.674	−3
19	−23.39	4.073	2.006	−2
20	−22.95	2.071	2.011	−1
21	24.15	5.925	1.996	+2
22	24.31	3.924	1.994	+1
23	24.79	1.922	1.988	+0
24	46.61	4.837	1.659	+2
25	56.97	5.784	1.492	+3
26	57.50	2.781	1.484	+1
27	68.53	3.707	1.318	+2
28	74.52	4.658	1.236	+3
29	78.31	5.623	1.188	+4
30	97.52	5.417	0.979	+5
31	98.03	4.411	0.974	+4
32	98.84	3.403	0.967	+3
33	100.3	2.387	0.954	+2
34	104.2	1.348	0.921	−1
35	117.6	5.236	0.825	−6
36	123.3	4.199	0.792	−5
37	133.5	3.145	0.743	−4
38	141.8	5.111	0.711	−7
39	160.5	4.051	0.665	−6
40	161.6	2.048	0.663	−3

[a]The + and − indicate a slow or fast solution, respectively.
[b]The second of two solutions on the same lower branch for the associated TOF.

One of the half-rev point sets and several of the full-rev circles have multiple labels. This is only true in the zero-point patched conic model. Using a more realistic model, a point on the velocity diagram cannot yield a true free-return trajectory if there is an intermediate encounter. Of course, in the real solar system the radius of a celestial body's sphere of influence is nonzero; thus, it is impossible to perform a flyby with a turning angle of zero. Consequently, $\boldsymbol{v}_\infty$ must rotate during a flyby. Technically, two consecutive half-rev returns on the same set of half-rev points are only possible in the realistic system if they are patched with a feasible flyby that rotates $\boldsymbol{v}_\infty$ from an x to an o or vice versa. Consecutive full-rev returns on the same full-rev circle are only possible if they are patched with feasible flybys and $\boldsymbol{v}_{\infty-} \neq \boldsymbol{v}_{\infty+}$. For the purposes of this study, the zero-point patched conic model assumptions hold. However, when transitioning solutions from this simple model to a more realistic one, the preceding comments should be considered.

In this example, the celestial body is in a noninclined, circular orbit. Thus, if a spacecraft leaves the body on an inclined circular orbit in the zero-point patched conic model, it will reencounter the body every half-revolution. This is why the middle x/o set is labeled with each half-year. Of course, this set also lies on the full-rev circle that corresponds to the celestial body's semimajor axis.

For any value of v_∞, a velocity diagram similar to Fig. 21 can be generated. The equations for the full-rev circles and the half-rev points are valid to find free returns to a celestial body in any

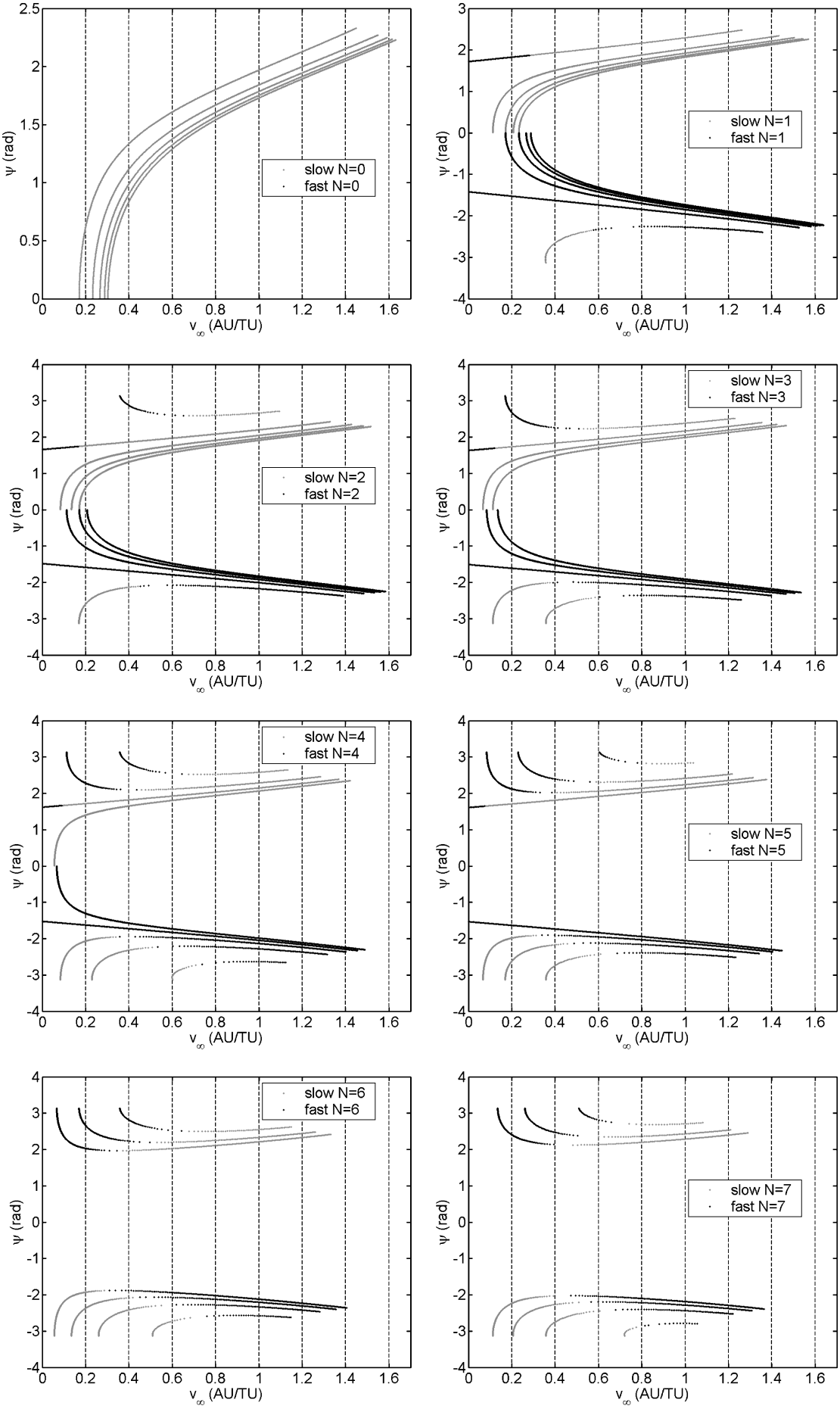

Fig. 17 Ψ vs v_∞ for generic returns to a body in circular orbit: $N = 0 \rightarrow 7$.

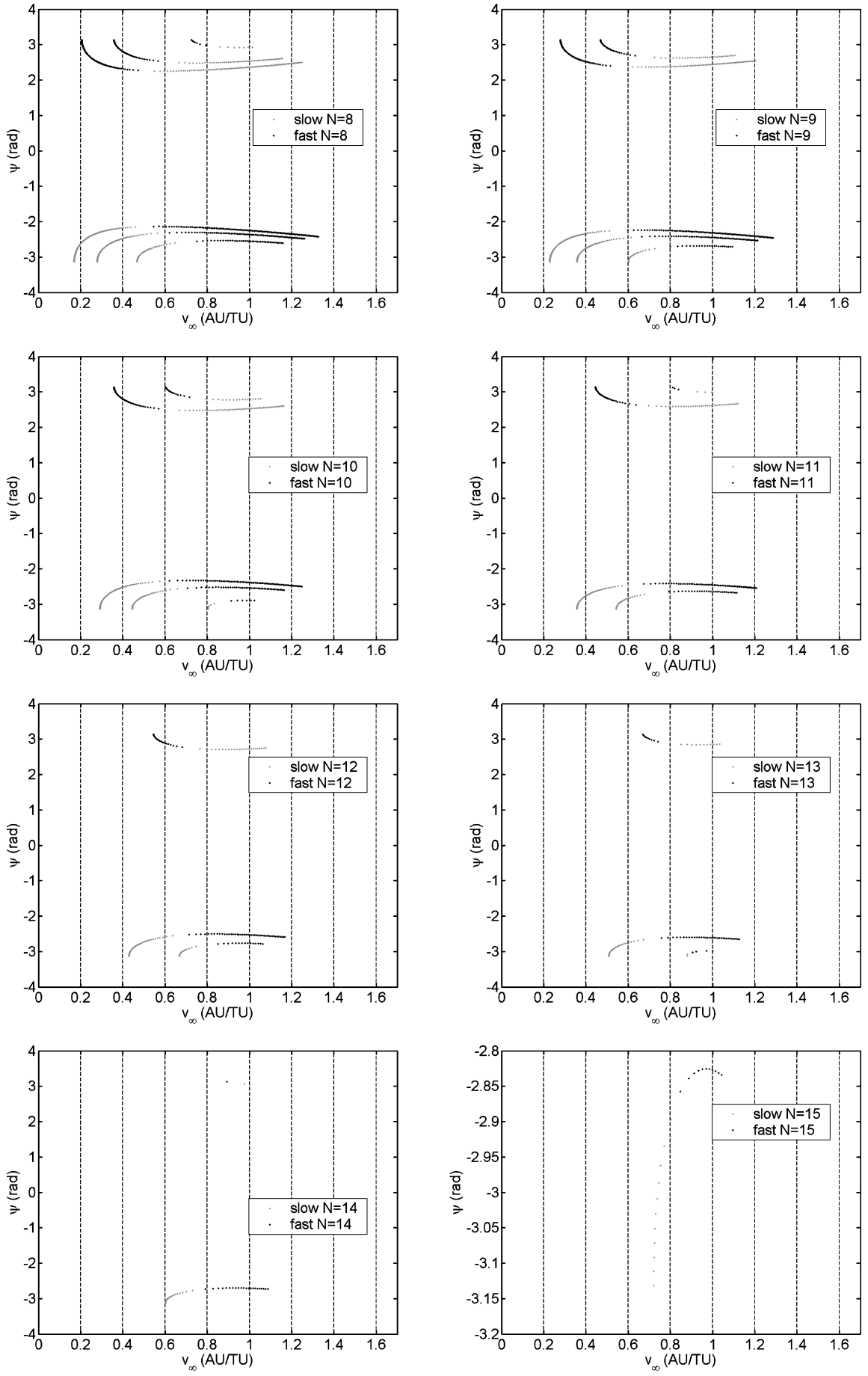

Fig. 18 Ψ vs v_∞ for generic returns to a body in circular orbit: $N = 8 \rightarrow 15$.

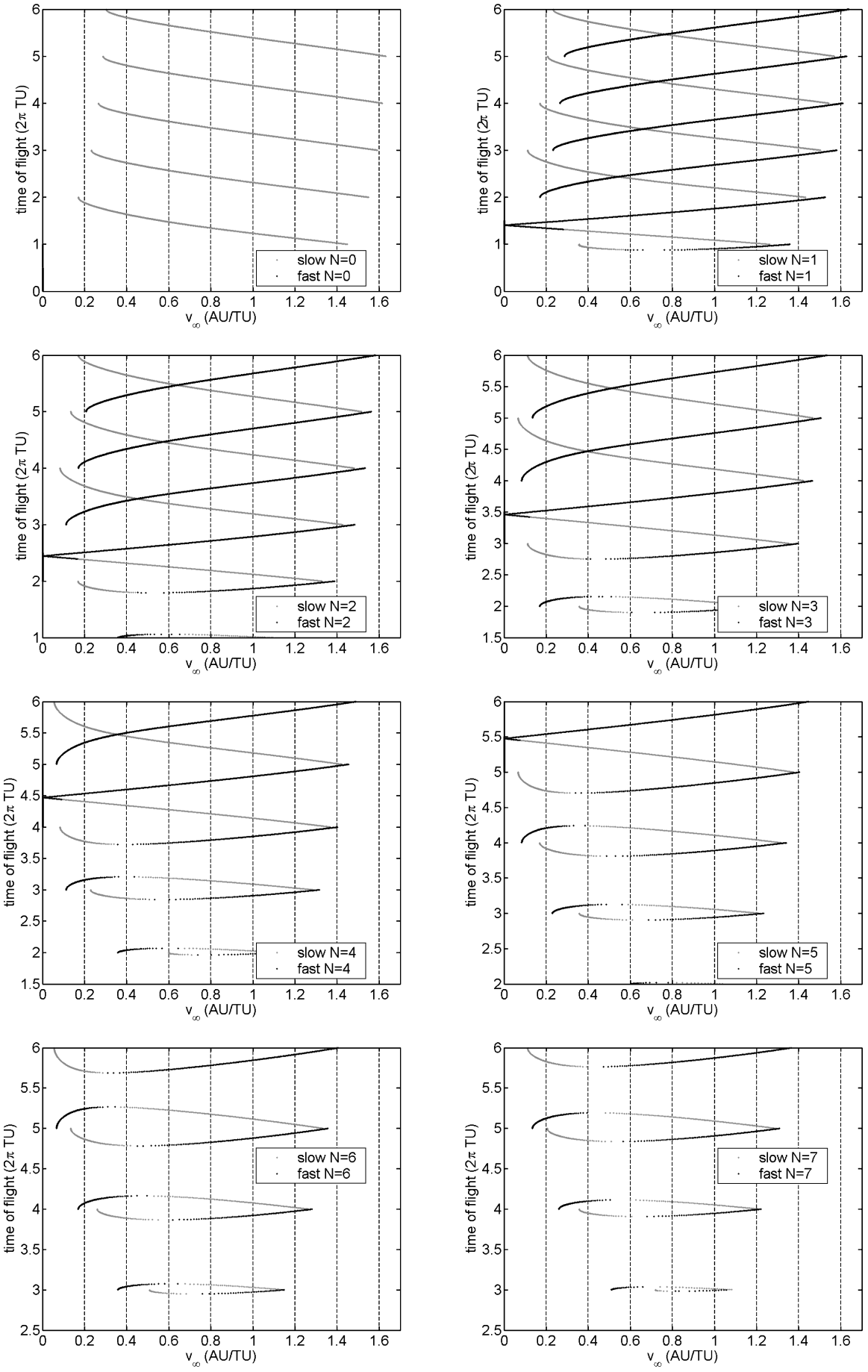

Fig. 19 TOF vs v_∞ for generic returns to a body in circular orbit: $N = 0 \rightarrow 7$.

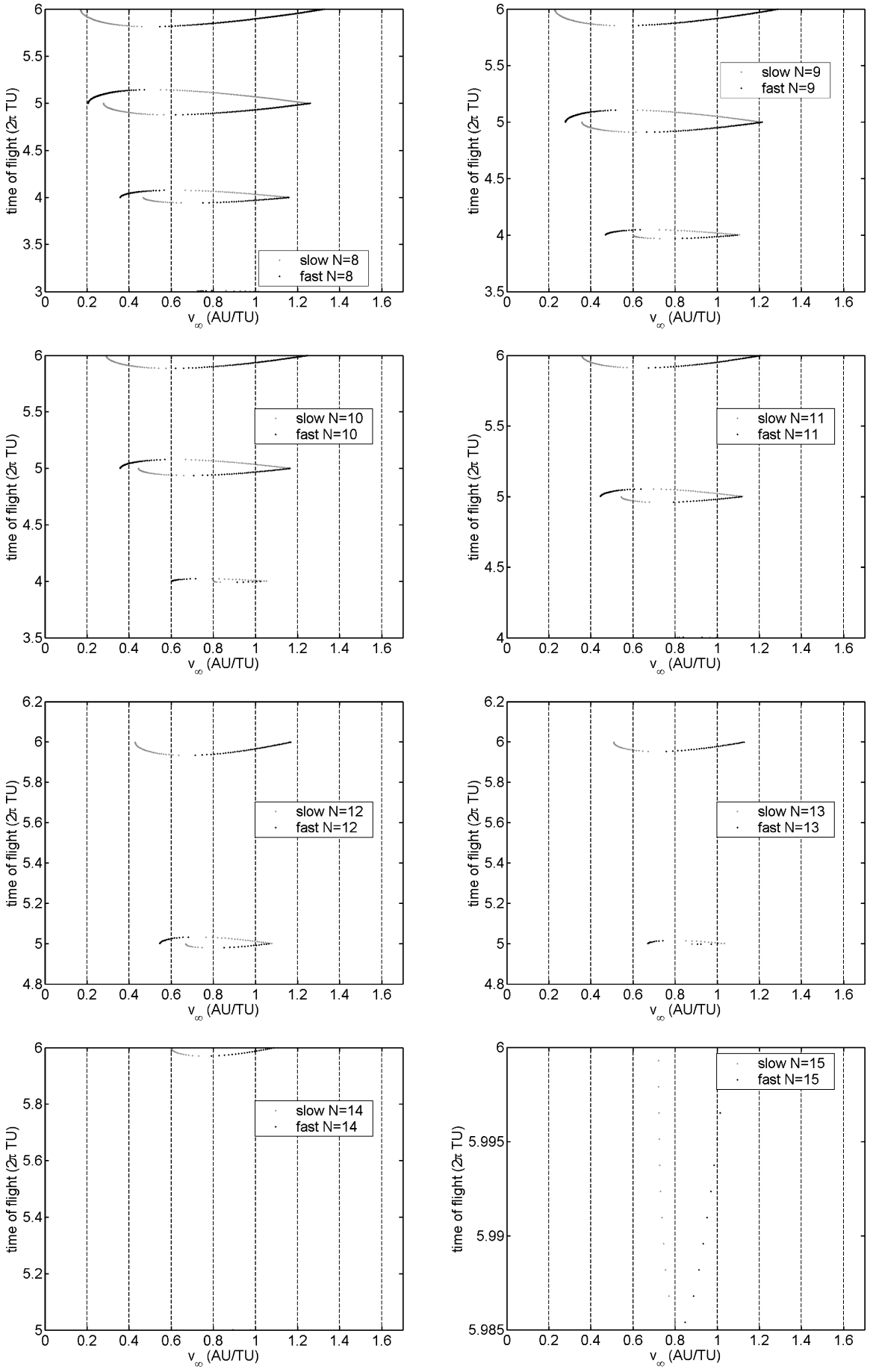

Fig. 20 TOF vs v_∞ for generic returns to a body in circular orbit: $N = 8 \rightarrow 15$.

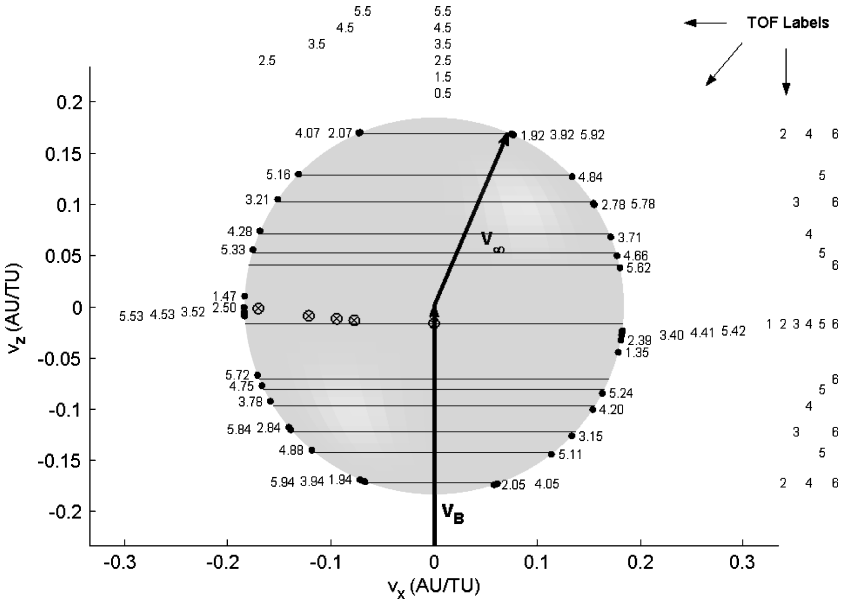

Fig. 21 Free-return solutions for $|v_\infty| = 0.1838$ AU/TU.

elliptic orbit. Remember, however, that the data in Figs. 17–20 must be regenerated in order to find the generic returns to a body in a noncircular orbit.

Numerical Considerations and Velocity Diagram Generation

The solutions for the full-revolution returns are analytic. Equation (17) gives the z coordinates for all full-revolution circles as a function of v_B, v_∞, and v_F, where all feasible values of v_F are found from Eqs. (13) and (14). Thus, the full-revolution circles on a velocity diagram are generated by plotting the circles described by Eq. (15) and feasible values of z.

The solutions for the half-revolution returns are both numerical and analytic. They are numerical in the sense that an iterative procedure is required to solve a Lambert problem to obtain the semimajor axis of the transfer orbit. A preceding section describes this problem in great detail. A variety of techniques are available that efficiently find all feasible solutions with accuracies on the order of machine precision.[14,15] Once the transfer semimajor axis values are known, solving for the half-revolution returns with a given v_∞ is analytically found using Eqs. (18), (19), and (23–25). Each valid semimajor axis leads to a pair of coordinates, and all nonimaginary pairs are the feasible half-revolution solutions. These coordinates are plotted on the velocity diagrams as sets of x/o points.

Unlike the half- or full-revolution return solutions, the generic-return solutions are entirely numerical in origin. As explained in detail, a Lambert problem is solved to find all free-returns to a celestial body at discrete time intervals up to a desired maximum time of flight. The solutions are then separated into common bins according to number of revolutions and whether they are fast or slow. Example properties of these families of solutions are given in Figs. 17–20. As the figures indicate, each family might contain several distinct subfamilies of solutions. Each subfamily is sorted according to v_∞, and finally the generic returns for a given v_∞ are found via interpolation. It is critical that the two neighboring interpolation points exist on the same subfamily of solutions: otherwise, the result is not valid. Thus, caution is advised when distinguishing between subfamilies of solutions.

In the limit as the time interval used to generate the original list of solutions goes to zero, the probability of skipping a solution and the error in the interpolation also approaches zero. The time interval used for this study is chosen to be sufficiently small such that decreasing the value does not increase the number of generic solutions found for arbitrary values of v_∞. This interval is then further reduced to provide additional confidence that no solutions will be skipped. The final value chosen, approximately a half-hour interval, provides over 180,000 solutions over a six-year time period. Thus, in order to find all generic returns with a given v_∞, an algorithm must sift through a nontrivial number of data points. The tips of the $\boldsymbol{v}_{\text{out}}$ vectors of the final solutions are plotted on the velocity diagrams as generic-return dots.

The accuracy of the final linearly interpolated solutions can be greatly improved by using them as initial guesses in a one-dimensional solver that fixes v_∞ and iterates on TOF and ψ in a Keplarian integration until the trajectory reencounters Earth to a desired tolerance. Thus, similar to the half- and full-revolution returns, the accuracy of these final generic-return solutions is also on the order of machine precision.

Cycler Applications

Applications for free returns include any flyby missions that require consecutive encounters with the same body. In particular, cycler missions are excellent applications because free-returns orbits are often used to satisfy the periodic time constraints.[4,10,11] For an orbit to be repeatable with respect to multiple celestial bodies, the period must be commensurate with the synodic period of the bodies. Free-returns can be used to loiter at a body without a powered maneuver until the timing is right to begin a new cycle. This method has been successful in finding Earth–Mars cycler orbits using half- and full-rev returns limited to 1π and 2π transfers respectively.[9–11] The analysis given here generalizes these terms to include all $n\pi$ transfers, which significantly expands the solution space when searching for ballistic cyclers.

Reference 11 lists many ballistic and near-ballistic Earth–Mars cyclers using Earth free-return orbits. Generic returns are patched together with 1π and 2π transfers such that the total cycler period is an integer multiple of the synodic period. The times of flight for the transfers were also limited to a half-year and full year, respectively. Many of the solutions require multiple consecutive 1π and 2π transfers that each must be patched with an Earth flyby. In many cases, several of the flybys become unnecessary if the $n\pi$ transfers are considered. The first four entries in Table 4 illustrate a few favorable examples. Take cycler 4.11.1.-2 as an example. The first number, 4, indicates it is a four synodic period cycler, and the second number, 11, indicates that the cycler must loiter at the Earth for 11 half-years before reinitiating the next cycle. In the method outlined in Ref. 11, the optimized solution is to perform four one-year transfers with three half-year transfers in the middle, all patched by Earth flybys. Alternatively, using the generalized definition for a half-rev transfer outlined in this paper, the seven free-return trajectories can be replaced with one 5.5-year half-rev return. Although the required turning angle increases to 107 deg, it still requires an Earth flyby altitude above 200 km. Because the half-rev loitering orbit is

Table 4 Examples of improved solutions to previously documented Earth–Mars cyclers

Cycler	Previous/new	v_∞ Earth, km/s	v_∞ Mars, km/s	Earth ↔ Mars transit time, days	Sequence of n half-year transfers patched by flybys	Turning angle for 200-km-alt. flyby, deg	Max turning angle req., deg
2.5.1. + 0[a]	Previous	7.8	9.9	94	2-1-2	60	54
	New	7.8	9.9	94	**5**	60	**61**
3.5.1 + 1[a]	Previous	5.4	9.2	115	2-1-2	84	73
	New	5.4	9.2	115	**5**	84	**69**
3.9.1. + 0[a]	Previous	5.4	9.2	116	2-2-1-2-2	84	72
	New	5.4	9.2	116	**9**	84	**82**
4.11.1. − 2[a]	Previous	3.6	4.7	195	2-2-1-1-1-2-2	111	70
	New	3.6	4.7	195	**11**	111	**107**
4.13.1. − 1[a]	Previous	5.5	9.3	137	2-2-2-1-2-2-2	84	72
	New	5.5	5.6	140	**4**-1-2-**6**	84	**79**
4.11.1. − 4[b]	Previous	——	——	——	——	——	——
	New	**3.8**	**4.8**	**168**	**2-6-2-1**	**108**	**87**

[a]Solutions documented in Ref. 11. [b]Solution found using methods outlined in Ref. 11 does not reach Mars.

not used for the Earth–Mars transfer, the energy characteristics of the cycler remain the same. On the contrary, the last two entries in Table 4 use three-year full-rev transfers in the ecliptic plane for the Earth–Mars transfer legs. Thus, the v_∞ at Mars are different, and significantly better in these cases, from the similar cyclers reported in Ref. 11. Cycler 4.13.1.-1 has a 40% decrease in v_∞ at Mars while increasing the transit time by only three days. Cycler 4.11.1.-4 did not come close to Mars using the methods described in Ref. 11, and thus it was not reported. However, using the general $n\pi$ transfers, a very attractive solution was found with a short transit time and low terminal speeds.

A full understanding of Table 4 requires a thorough reading of Ref. 11. However, the purpose of this section is not to detail the origin of Table 4, but rather to illustrate an example application for the diagrams similar to Fig. 21. A future study will expand on the examples above and give a detailed procedure to apply the methods presented in this paper to the search for cycler orbits.

Conclusions

Noting that several recent studies found practical applications for free-returns that included 1π and 2π transfers for the spacecraft and the celestial body, it was observed that much could be gained if the idea were generalized to include $n\pi$ transfers. The semimajor axis values for the even-$n\pi$ free-return transfers, or full-rev returns, are derived both with a simple approach and taking the limit as $\boldsymbol{r}_1$ approaches $\boldsymbol{r}_2$ in Lambert's problem. Several interesting properties of the Lambert solutions are noted including the obviously impractical rectilinear ellipse solution. The semimajor axis values for the odd-$n\pi$ and the generic free-return transfers can only be found using Lambert's equation because the times of flight are not integer multiples of orbital periods.

In velocity space, all solutions for a given half-rev return are shown to lie on a set of constant-diameter circles forming a tube, whereas all solutions for a given full-rev return are shown to lie on multiple concentric spheres. The solutions for the generic returns are shown to lie on a series of nonuniform arcs in the ecliptic plane. Intersections of these lines and surfaces with the flyby sphere of constant v_∞ identifies the half-rev points, full-rev circles, and generic return dots of intersection that lead to potential free-return transfers following a flyby. The equations for the locations of the full-rev circles and sets of half-rev points are derived, and a numerical method is outlined to find the locations for all generic return dots.

When including the possibility of multiple body and spacecraft revolutions, the final result is the common three-dimensional v_∞ sphere with a surface marked by all feasible free-return solutions. The generation of such a diagram is straightforward, based on the geometry of the celestial body's orbit and the hyperbolic energy of the spacecraft. These diagrams are useful mission design tools for any application requiring consecutive flybys of the same body.

Although a detailed analysis of applying the $n\pi$ transfers to finding interplanetary cyclers is left to future work, this paper presents several samples of new and/or improved Earth–Mars cyclers that include the generalized half- and full-rev free returns. An effort is currently underway to find and catalog other idealized Earth–Mars cyclers using the described solutions.

Acknowledgments

A special thanks is owed to the Flight Dynamics Analysis Branch at NASA's Goddard Space Flight Center for providing a Graduate Student Researchers Program Fellowship. We also are grateful to Troy McConaghy of Purdue University for his assistance with the three-dimensional visualization.

References

[1]Patel, M. R., Longuski, J. M., and Sims, Jon A., "Mars Free Return Trajectories," *Journal of Spacecraft and Rockets*, Vol. 35, No. 3, 1998, pp. 350–354.

[2]Miele, A., Wang, T., and Mancuso, S., "Optimal Free-Return Trajectories for Moon Missions and Mars Missions," *Journal of the Astronautical Sciences*, Vol. 48, No. 2–3, 2000, pp. 183–206.

[3]Wolf, A. A., "Free-Return Trajectories for Mars Missions," American Astronautical Society, AAS Paper 91-123, Feb. 1991.

[4]Hollister, W. M., "Periodic Orbits for Interplanetary Flight," *Journal of Spacecraft and Rockets*, Vol. 6, No. 4, 1969, pp. 366–369.

[5]Uphoff, C. W., "The Art and Science of Lunar Gravity Assist," *Advances in Astronautical Sciences, Vol. 69, Orbital Mechanics and Mission Design*, edited by J. Teles, Univelt, Inc., San Diego, CA, 1989, pp. 333–346.

[6]Uphoff, C., and Crouch, M. A., "Lunar Cycler Orbits with Alternating Semi-Monthly Transfer Windows," *Journal of the Astronautical Sciences*, Vol. 41, No. 2, 1993, pp. 189–205.

[7]Uphoff, C., Roberts, P. H., and Friedman, L. D., "Orbit Design Concepts for Jupiter Orbiter Missions," *Journal of Spacecraft and Rockets*, Vol. 13, No. 6, 1976, pp. 348–355.

[8]Menning, M. D., "Freefall Periodic Orbits Connecting Earth and Venus," M.S. Thesis, Dept. of Aeronautics and Astronautics, Massachusetts Inst. of Technology, Cambridge, MA, July 1968.

[9]Rall, C. S., "Freefall Periodic Orbits Connecting Earth and Mars," Ph.D. Dissertation, Dept. of Aeronautics and Astronautics, Massachusetts Inst. of Technology, Cambridge, MA, Oct. 1969.

[10]Byrnes, D. V., McConaghy, T. T., and Longuski, J. M., "Analysis of Various Two Synodic Period Earth-Mars Cycler Trajectories," American Astronautical Society, AAS Paper 2002-4423, Aug. 2002.

[11]Russell, R., and Ocampo, C., "Systematic Method for Constructing Earth–Mars Cyclers Using Free-Return Trajectories," *Journal of Guidance, Control, and Dynamics*, Vol. 27, No. 3, 2004, pp. 321–335.

[12]Prussing, J. E., and Conway, B. A., *Orbital Mechanics*, Oxford Univ. Press, New York, 1993. pp. 63–80.

[13]Battin, R. H., *An Introduction to the Mathematics and Methods of Astrodynamics*, rev. ed., AIAA, Reston, VA, 1999, p. 241.

[14]Prussing, J. E., "A Class of Optimal Two-Impulse Rendezvous Using Multiple-Revolution Lambert Solutions," *Journal of the Astronautical Sciences*, Vol. 48, Nos. 2 and 3, 2000, pp. 131–148.

[15]Shen, H., and Tsiotras, P., "Using Battin's Method to Obtain Multiple-Revolution Lambert's Solutions," American Astronautical Society, AAS Paper 03-568, Aug. 2003.

C. McLaughlin
Associate Editor